Reversing Berry phase and modulating Andreev reflection by Rashba spin-orbit coupling in graphene mono- and bilayers

Xuechao Zhai and Guojun Jin*

National Laboratory of Solid State Microstructures and Department of Physics, Nanjing University, Nanjing, 210093, China

(Received 2 December 2013; revised manuscript received 19 February 2014; published 28 February 2014)

Graphene with Rashba spin-orbit coupling (RSOC) has attracted much attention so far. However, no one has noticed the topologically nontrivial changes of Berry phase for RSOC from the absence to the presence. We demonstrate that the Berry phase of electronic wave functions changes from π to 2π in graphene monolayer (GML) and from 2π to π in graphene bilayer (GBL), driven by RSOC. These reversals of Berry phase result in anomalous electron-hole conversions at normal conductor-superconductor junctions. The specular Andreev reflection can be significantly reduced in GML, but obviously enhanced in GBL. Another unusual point caused by RSOC is that the spin-flipped electron reflection happens due to the spin helical structures on equal-energy surfaces. An electrically observable effect induced by RSOC is proposed such that the differential conductance at voltages below the superconducting gap decreases strongly for GML while it increases remarkably for GBL, attributed to the Berry-phase-dictated interference between incident and reflected states.

DOI: 10.1103/PhysRevB.89.085430 PACS number(s): 74.45.+c, 73.23.−b, 71.70.Ej

I. INTRODUCTION

In the past decade, one-atomic thick graphene with honeycomb structure has become a promising arena for verifying several significant phenomena in fundamental physics and providing many foreseeable applications in nanoelectronics [1,2]. One of the most important findings is that the electronic states in graphene monolayer (GML) and graphene bilayer (GBL) exhibit, respectively, Berry phases of π and 2π, giving rise to their entirely different behaviors in electron tunnelings [3] and quantum Hall effects [4,5]. Associated with the π-Berry phase in GML, a striking phenomenon, the specular Andreev reflection, has been found at a normal conductor-superconductor (NS) junction [6], when the Fermi wavelength in the weakly doped region N is larger than the superconducting coherence length. This differs very much from the conventional process of the Andreev retroreflection. The signal of the specular Andreev reflection in GBL, however, is very weak [7], due to the 2π-Berry phase. Experimentally, the Andreev reflections may be detected in a superconducting device [8], where the superconducting state is introduced in graphene from the proximity with a superconducting substrate. Further theoretical work has shown that finite width can change drastically the NS behavior [9–11] and the magnetic correlation can enhance the specular Andreev reflection [12–15] in graphene.

Recently, the specular Andreev reflection has also been discussed at an NS junction in a two-dimensional electron gas with Rashba spin-orbit coupling (RSOC), for the different topological structures of equal-energy surfaces of electrons and holes [16]. For a GML with RSOC, the spin helical structures on equal-energy surfaces [17] have been shown. Through theoretical treatment, we notice that the GML and GBL with RSOC have basically the same spin helical structures on equal-energy surfaces. Our further analysis indicates that both of them exhibit the RSOC-driven topological changes, characterized by the changes of their Berry phase, from π to 2π for GML and from 2π to π for GBL. Considering the strong dependence of Andreev reflections on band topology, we would like to make clear the electron-hole conversions at an NS junction in the presence of RSOC. The NS device is illustrated in Fig. 1, where the RSOC in the level of 10 meV can be applied in the region N and can be realized in experiment by placing a GML (GBL) in Ni(111) substrate, with an Au monolayer intercalated [18]. Alternatively, through doping with adatoms [19], the RSOC may be applied as well.

By solving the Bogoliubov-de Gennes (BdG) equation of superconductivity [6,7], we find that the specular Andreev reflection is completely suppressed by RSOC in GML while observably enhanced in GBL, when the region N is weakly doped, attributed to the interference between incident and reflected states. This leads to a measurable effect that the differential conductance at voltages below the superconducting gap is strongly decreased by RSOC for GML but significantly increased for GBL. These results originate from the RSOC-driven nontrivial changes of the Berry phase. This paper is organized as follows. In Sec. II, we give the spinor structures of GML and GBL and argue the topological properties characterized by the Berry phase. The phenomena of the Andreev reflections are discussed in Sec. III, and the differential conductance is given in Sec. IV. A summary is presented in Sec. V.

II. SPINOR STRUCTURES OF ELECTRONIC STATES

In this section, for simplicity, we discuss the Hamiltonian and electronic states when the GML and GBL are undoped, i.e., the Fermi energy is zero. Certainly, the nonzero Fermi energy does not alter our main conclusions.

Graphene monolayer. A GML is constructed of two trigonal sublattices A, B. In the basis $\{\psi_{A\uparrow},\psi_{A\downarrow},\psi_{B\uparrow},\psi_{B\downarrow}\}$, the effective Hamiltonian of an undoped GML with the RSOC for one valley is written as

$$\mathcal{H}_\xi = \hbar v_F(\sigma_x k_x + \xi\sigma_y k_y)\otimes s_0 + \frac{\lambda_R}{2}(\sigma_x\otimes s_y - \xi\sigma_y\otimes s_x), \quad (1)$$

*gjin@nju.edu.cn

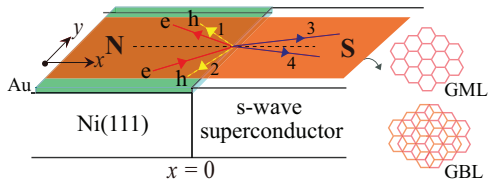

FIG. 1. (Color online) Schematic of an NS junction, based on a GML or GBL. The Rashba region N is experimentally realized by placing a GML or GBL in Ni(111) substrate, with an Au monolayer intercalated, and the region S contacts with an *s*-wave superconductor. The possible interface scattering processes are sketched, including the specular Andreev reflection (1), Andreev retroreflection (2), and transmissions of electronlike (3) and holelike (4) BdG-quasiparticles.

where $\mathcal{H}_\xi$ is divided into two parts $\mathcal{H}_\xi = H_\xi^0 + \mathcal{H}_\xi^{\rm R}$. The first term H_ξ^0 is the intrinsic term, and the second term $\mathcal{H}_\xi^{\rm R}$ is the Rashba term. The notation $\xi = +(-)$ indicates valley K (K′), the constant $v_{\rm F} = 10^6$ ms^{-1} is the Fermi velocity [3,5], and $\lambda_{\rm R}$ is the Rashba parameter. The 2×2 Pauli matrices (σ_x, σ_y), (s_x, s_y) are in the pseudospin, real-spin spaces, with the unit matrices denoted by σ_0, s_0. The Hamiltonian (1) is the low-energy approximation of the tight-binding Hamiltonian [17,20].

The whole Hamiltonian including the two valleys reads

$$\mathcal{H} = \begin{pmatrix} \mathcal{H}_+ & 0 \\ 0 & \mathcal{H}_- \end{pmatrix}, \tag{2}$$

which is time-reversal invariant, i.e., $\mathcal{T}\mathcal{H}\mathcal{T}^{-1} = \mathcal{H}$. The time reversal operator can be given as

$$\mathcal{T} = i \begin{pmatrix} 0 & \sigma_z \otimes s_y \\ \sigma_z \otimes s_y & 0 \end{pmatrix} C, \tag{3}$$

with σ_z the Pauli matrix for pseudospin and C the operator of complex conjugation. One can verify $\mathcal{T}^2 = -1$, which is a necessary property satisfied by fermions [21].

By solving the stationary equation $\mathcal{H}\psi = E\psi$, we obtain the eigenvalues as

$$E_{\mu\nu}(k) = \frac{\mu\nu}{2}\left(\sqrt{\lambda_{\rm R}^2 + 4(\hbar v_{\rm F} k)^2} - \nu\lambda_{\rm R}\right), \tag{4}$$

where $\mu, \nu = \pm$ can distinguish four different subbands. The wave vector modulus satisfies $k = \sqrt{k_x^2 + k_y^2}$. At a given μ, the spinor wave vectors read

$$\begin{aligned}
\psi_{\mu+}^{\rm K} &= c_0(i\mu\varrho e^{-i\theta}, \mu\varrho', i\varrho', \varrho e^{i\theta})^{\rm T}, \\
\psi_{\mu-}^{\rm K} &= c_0(i\mu\varrho' e^{-i\theta}, -\mu\varrho, -i\varrho, \varrho' e^{i\theta})^{\rm T}, \\
\psi_{\mu+}^{\rm K'} &= c_0(\mu\varrho', -i\mu\varrho e^{i\theta}, \varrho e^{-i\theta}, -i\varrho')^{\rm T}, \\
\psi_{\mu-}^{\rm K'} &= c_0(-\mu\varrho, -i\mu\varrho' e^{i\theta}, \varrho' e^{-i\theta}, i\varrho)^{\rm T},
\end{aligned} \tag{5}$$

where the superscript T represents the transpose, $c_0 = 1/\sqrt{2}$ is the normalized constant, and $\theta = \arctan(k_y/k_x)$ is the angle of the wave vector $\boldsymbol{k}$. It is defined that $\varrho = \cos(\vartheta/2)$, $\varrho' = \sin(\vartheta/2)$ with $\vartheta = \arctan(2\hbar v_{\rm F} k/\lambda_{\rm R})$. The expectations of the real-spin operator $\sigma_0 \otimes s$ and the pseudospin operator $\sigma \otimes s_0$

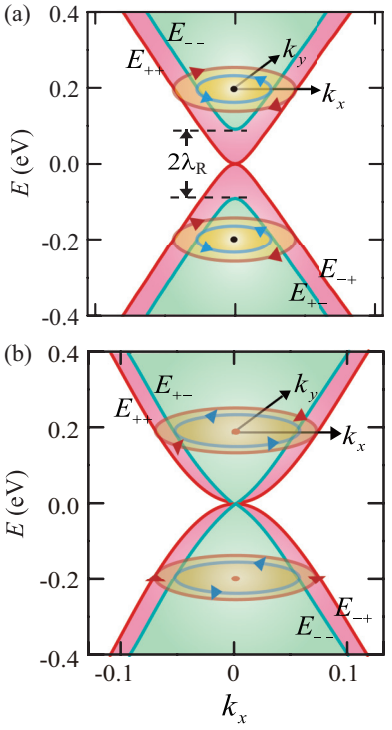

FIG. 2. (Color online) Band structures of an undoped (a) GML and (b) GBL under RSOC in the vicinity of valley K (identical for valley K′), given by Eqs. (4) and (10), respectively. The red (green) boundary lines between different background colors indicate the outer (inner) subbands relative to the central axis $k_x = 0$. Each subband energy is labeled by $E_{\mu\nu}$, where μ, ν take the signs $\pm$. The value $2\lambda_{\rm R}$ in (a) denotes an energy splitting at the point K (K′). The circles with arrows in (a) and (b) sketch the spin helical structures of equal-energy surfaces in the (k_x, k_y) plane.

are given as

$$\langle \sigma_0 \otimes s \rangle_{\mu\nu} = \nu \sin\vartheta(\boldsymbol{x}\sin\theta - \boldsymbol{y}\cos\theta) = (\boldsymbol{e}_k \times \boldsymbol{z})\nu\sin\vartheta, \tag{6}$$

$$\langle \sigma \otimes s_0 \rangle_{\mu\nu} = \mu\nu \sin\vartheta[\boldsymbol{x}\cos\theta + \boldsymbol{y}\sin\theta] = \boldsymbol{e}_k \mu\nu \sin\vartheta, \tag{7}$$

where $\sin\vartheta = 2\hbar v_F k/\sqrt{\lambda_{\rm R}^2 + 4(\hbar v_{\rm F} k)^2}$ and $\boldsymbol{e}_k = \boldsymbol{k}/k$. In Eq. (6), the sign of ν signifies the helical direction of the real spin, as sketched in Fig. 2(a), identical for valleys K and K′. In Eq. (7), the sign of $\mu\nu$ determines the orientation of the pseudospin polarization vector $\boldsymbol{e}_k$.

To characterize the global property of the pseudospin and real-spin under the RSOC, we give the Berry phase [22] of the electronic states in Eq. (5) as

$$\Phi_{\rm B} = i\int_0^{2\pi} d\theta \langle \psi_{\mu\nu}^\xi | \frac{\partial}{\partial\theta} | \psi_{\mu\nu}^\xi \rangle = 0. \tag{8}$$

One can verify that, using another gauge by multiplying $\psi_{\mu\nu}^\xi$ by $e^{-i\theta}$ [22,23], $\Phi_{\rm B}$ in Eq. (8) becomes 2π. Nevertheless, this gauge only changes the winding number of the pseudospin [23]. It means that the values of Berry phases 0 and 2π are topologically equivalent. It is understood that, in GML without RSOC, the singularity of the Dirac node leads to a

π-Berry phase [24]. Driven by RSOC, the node is removed, because the relation of $E_{\mu\nu}$ versus k in Eq. (4) changes from the original linear odd function to an even function. The subbands E_{++}, E_{-+} in Fig. 2(a) only touch each other at zero energy but do not cross. Hence, a topological change is driven by RSOC, with the Berry phase changed from π (for $\lambda_R = 0$) to 2π (for $\lambda_R \neq 0$).

Graphene bilayer. A Bernal-stacked GBL consists of two coupled GMLs, with inequivalent sublattices A, B and $\tilde{A}$, $\tilde{B}$ on the top and bottom layers, respectively. The interlayer coupling $\gamma = 0.39$ eV [25,26] exists between A and $\tilde{B}$. Under the RSOC, the full Hamiltonian constructed from two 4×4 matrices in Eq. (1) is an 8×8 matrix. Using perturbation method under low-energy condition $E < \gamma$ [27,28], an effective 4×4 Hamiltonian is derived to describe four low-energy subbands,

$$\begin{aligned}\mathcal{H}_\xi &= H_\xi^0 + H_\xi^R \\ &= -\frac{(\hbar v_F k)^2}{\gamma}\begin{pmatrix} 0 & e^{-2i\xi\theta} \\ e^{2i\xi\theta} & 0 \end{pmatrix} \otimes s_0 - \frac{\hbar v_F \lambda_R}{\gamma} \\ &\quad \times [\sigma_x \otimes (k_x s_y + k_y s_x) - \xi \sigma_y \otimes (k_x s_x - k_y s_y)], \end{aligned} \tag{9}$$

where $\{\psi_{\tilde{A}_\uparrow}, \psi_{\tilde{A}_\downarrow}, \psi_{B_\uparrow}, \psi_{B_\downarrow}\}$ is the basis. The time-reversal invariance $\mathcal{T}\mathcal{H}\mathcal{T}^{-1} = \mathcal{H}$ can be verified using Eqs. (2) and (3).

By solving the equation $\mathcal{H}\psi = E\psi$ for the undoped GBL, the eigenvalues are given as

$$E_{\mu\nu}(k) = \frac{\mu\hbar v_F k}{\gamma}\left(\sqrt{\lambda_R^2 + (\hbar v_F k)^2} - \nu\lambda_R\right). \tag{10}$$

Here, $\mu, \nu = \pm$ distinguishes four subbands, as labeled in Fig. 2(b). The eigenvectors read

$$\begin{aligned} \psi_{\mu+}^K &= c_0(-i\mu\varrho e^{-2i\theta}, -\mu\varrho' e^{-i\theta}, i\varrho', \varrho e^{i\theta})^T, \\ \psi_{\mu-}^K &= c_0(i\mu\varrho' e^{-2i\theta}, -\mu\varrho e^{-i\theta}, -i\varrho, \varrho' e^{i\theta})^T, \\ \psi_{\mu+}^{K'} &= c_0(-\mu\varrho' e^{i\theta}, i\mu\varrho e^{2i\theta}, \varrho e^{-i\theta}, -i\varrho')^T, \\ \psi_{\mu-}^{K'} &= c_0(-\mu\varrho e^{i\theta}, -i\mu\varrho' e^{2i\theta}, \varrho' e^{-i\theta}, i\varrho)^T, \end{aligned} \tag{11}$$

where $\varrho = \cos(\vartheta/2)$, $\varrho' = \sin(\vartheta/2)$ with $\vartheta = \arctan(\hbar v_F k/\lambda_R)$, distinct from those definitions in Eq. (5) for GML. Expectations of the real-spin operator $\sigma_0 \otimes s$ and the pseudospin operator $\sigma \otimes s_0$ are given as

$$\langle \sigma_0 \otimes s \rangle_{\mu\nu} = (\boldsymbol{e}_k \times \boldsymbol{z})\nu \sin\vartheta, \tag{12}$$

$$\langle \sigma \otimes s_0 \rangle_{\mu\nu} = -\mu \sin\vartheta [\boldsymbol{x}\cos(2\theta) + \xi \boldsymbol{y}\sin(2\theta)]. \tag{13}$$

The spin helicities and pseudospin polarizations here are, respectively, related to the signs of ν in Eq. (12) and μ in Eq. (13). Under the RSOC, the spin helical properties for GBL are sketched in Fig. 2(b), which exhibits basically the same characteristics as shown in Fig. 2(a) for GML.

The Berry phase of $\psi_{\mu\nu}^\xi$ in GBL with RSOC reads

$$\Phi_B = i\int_0^{2\pi} d\theta \langle \psi_{\mu\nu}^\xi | \frac{\partial}{\partial\theta} | \psi_{\mu\nu}^\xi \rangle = \begin{cases} \pi, & \text{for } \psi_{\mu\nu}^K \\ -\pi, & \text{for } \psi_{\mu\nu}^{K'}, \end{cases} \tag{14}$$

different from 2π in GBL without RSOC [4,23], where no node exists in a parabolic even function $E(k)$. Under the RSOC, a node appears at zero energy because $E_{\mu\nu}$ in Eq. (10) is an odd function of k and the subbands E_{++}, E_{-+} (E_{+-}, E_{--}) in Fig. 2(b) cross each other. Thus, a topologically nontrivial change is driven by RSOC, with the Berry phase changed from 2π (for $\lambda_R = 0$) to π (for $\lambda_R \neq 0$). Interestingly, the Berry phase for GBL with RSOC turns into the value for GML without RSOC. For a graphene N layer, the Berry phase is to be changed from $N\pi$ without RSOC [29] to $(N-1)\pi$ under the RSOC.

III. ANDREEV REFLECTION AT AN NS JUNCTION

Now, we consider the electron-hole conversion at the interface of an NS junction, where the RSOC is present only in the region N of GML (GBL), as illustrated in Fig. 1. The excitations of quasiparticles from the regions N and S can be described by the BdG equation, $\mathcal{H}\psi(\boldsymbol{r}) = \varepsilon\psi(\boldsymbol{r})$. In the Nambu space, the spinor basis reads $\psi = (u, \upsilon)^T = [(\psi_{\mathcal{A}_\uparrow}, \psi_{\mathcal{A}_\downarrow}, \psi_{B_\uparrow}, \psi_{B_\downarrow})^\xi, (-\psi_{\mathcal{A}_\downarrow}^*, \psi_{\mathcal{A}_\uparrow}^*, \psi_{B_\downarrow}^*, -\psi_{B_\uparrow}^*)^{\bar{\xi}}]^T$, where $\mathcal{A}$ indicates the sublattice A ($\tilde{A}$) for GML (GBL), $\bar{\xi} = -\xi$, and $\upsilon = \mathcal{T}u$. Due to the valley degeneracy, the BdG equation can be decoupled and then written as

$$\begin{pmatrix} \mathcal{H}_\xi(x) - E_F & \Delta\Theta(x) \\ \Delta^*\Theta(x) & E_F - \mathcal{H}_\xi(x) \end{pmatrix}\begin{pmatrix} u \\ \upsilon \end{pmatrix} = \varepsilon\begin{pmatrix} u \\ \upsilon \end{pmatrix}, \tag{15}$$

where the position-dependent Hamiltonian reads $\mathcal{H}_\xi(x) = \mathcal{H}_\xi^0 + \mathcal{H}_\xi^R\Theta(-x) - U_0\Theta(x)$, with $\Theta(x)$ the Heaviside step function. In comparison with Eqs. (1) and (9), the Fermi energy E_F here is a variable tuned by a gate. The potential $-U_0\Theta(x)$ gives the relative shift of E_F in N and S, and can be adjusted by an additional gate voltage or doping. In S, the s-wave superconducting pair potential $\Delta = \Delta_0 e^{i\phi}$ is used, and a fixed value $\Delta_0 = 1$ meV is assumed. Of course, a larger pair potential should lead to easier observable results.

The use of a sharp Heaviside step potential at the interface is based on such an approximation that Δ reaches its value at a negligible distance from the interface. This requires the Fermi wavelength in S should be much smaller than the value in N [6]. Meanwhile, to ensure the validity of the mean-field approximation, phase fluctuations of the order parameter should be small. This requires the Fermi wavelength in S should be much smaller than the superconducting coherent length [6,7], or equivalently the energy relation $E_F' = (E_F + U_0) \gg \Delta_0$. In our calculations, a highly doped condition $E_F' = 300\Delta_0$ is adopted in S. Because the equal-energy surfaces are identical for the two valleys, as sketched in Fig. 2, electrons in either valley follows the same incident/reflection trajectory. Hence we only need to consider the case of incidence in valley K.

In the case of $E_F < |E - E_F|$ (E is the incident energy of electron) and $\lambda_R = 0$, the specular Andreev reflection in Fig. 1 happens: The conduction-band electron is incident and the valence-band hole is reflected. The signal of the specular Andreev reflection has been proved to be very strong in GML [6] due to the electron-hole constructive interference induced by the π-Berry phase, but very weak in GBL [7] because of the electron-hole destructive interference induced by the 2π-Berry phase. In the case of $\lambda_R \neq 0$, the specular Andreev reflection should be reduced in GML with the 2π-Berry phase, but enhanced in GBL with the π-Berry phase.

In the following, we discuss the Andreev reflections in detail for GML and GBL with RSOC, respectively.

Graphene monolayer. By solving the BdG equation in GML, the excitation spectrum of quasiparticles in N ($x < 0$) can be given as

$$\varepsilon_{\mu\nu} = \tfrac{1}{2}\left|\sqrt{\lambda_R^2 + 4(\hbar v_F k)^2} - \nu\lambda_R - 2\mu\nu E_F\right|. \quad (16)$$

In comparison with Eq. (4), $\varepsilon_{\mu\nu} = |E_{\mu\nu}(k) - E_F| > 0$. This means that the excited quasiparticles comes from the conduction (valence) bands in Fig. 2(a) when $E_{\mu\nu} > E_F (E_{\mu\nu} < E_F)$. Because the Hamiltonian simplifies to $\mathcal{H}_\xi(x > 0) = \mathcal{H}_\xi^0 - E_F'$ in S, the excitation spectrum of the BdG quasiparticles can be obtained as $\varepsilon_{\mu\nu} = \sqrt{\Delta_0^2 + (E_F' + \mu\nu \cdot \hbar v_F k)^2}$. In both N and S, all the incident and interface-scattering states $(u,v)\exp(i\boldsymbol{k}\cdot r)$ in the Nambu space could be solved from Eq. (15). Using the continuity of the wave functions at $x = 0$, the reflection amplitudes can be calculated in principle. Because the wave functions depend on both the modulus and angles of wave vectors here, it greatly increases the complexity to analytically solve the reflection amplitudes, and thus numerical calculations are performed to obtain the useful results.

We are mainly concerned with the Andreev reflections when the region N is within the weakly doped regime I ($E_F < \Delta_0 < \lambda_R$) and the strongly doped regime II ($E_F' \gg E_F > \lambda_R \gg \Delta_0$), as discussed previously [6,7]. For the former, the specular Andreev reflection is present when $\varepsilon > E_F$ and the Andreev retroreflection is present when $\varepsilon < E_F$; for the latter, only Andreev retroreflection happens because $\varepsilon \ll E_F$. The incident and reflected particles, as described in Fig. 1, should satisfy (i) energy conservation, (ii) momentum conservation in the y direction, and have (iii) opposite directions of their group velocities in the x direction. According to these conditions, Figs. 3(a) and 3(b) plot the momenta of all possible incident and reflected states on the equal-energy surfaces (denoted by circular contours) for $E_F = 0$ and $E_F \gg \Delta_0$, respectively: ψ_a is the only incident state in regime I and lies in subband $(\mu,\nu) = (+,+)$, while $\psi_{a'}$ in subband $(-,-)$ denotes the other incident state (except ψ_a) in regime II; ψ_b and $\psi_{b'}$ describe the intravalley reflected electron states for ψ_a or $\psi_{a'}$; ψ_c in subband $(-,+)$ [valence band in Fig. 2(a)] is the intervalley specular Andreev-reflection state for ψ_a in regime I, while ψ_c, $\psi_{c'}$ in subbands $(+,+),(-,-)$ [conduction band in Fig. 2(a)] indicate the intervalley Andreev-retroreflection states for ψ_a or $\psi_{a'}$ in regime II. It can be further proved that the specular Andreev reflection state satisfies $v_{g,y} = (1/\hbar)\partial\varepsilon/\partial k_y > 0$, while the Andreev retroreflection state satisfies $v_{g,y} < 0$.

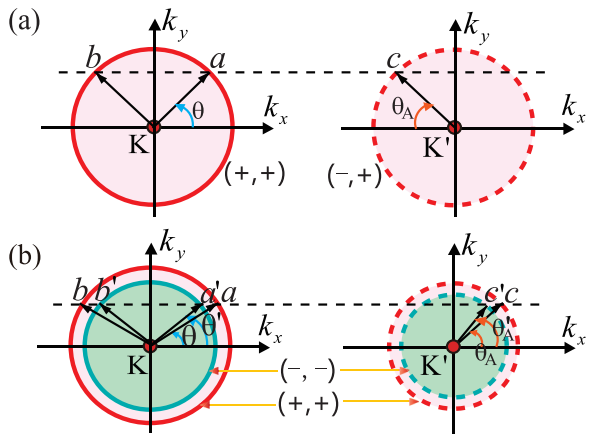

FIG. 3. (Color online) (a) and (b) Equal-energy surfaces of GML shown by the circular contours labeled with (μ,ν), given by Eq. (16), under $E_F = 0 \ll \Delta_0$ and $E_F \gg \Delta_0$, respectively. For the incident states ψ_a and $\psi_{a'}$, reflected states ψ_b and $\psi_{b'}$, Andreev reflection states ψ_c and $\psi_{c'}$, their momenta, and angles in the (k_x,k_y) plane are marked. The horizontal dashed lines indicate the momentum conservation, and all the reflected states can be proved to satisfy $v_{g,x} = (1/\hbar)\partial\varepsilon/\partial k_x < 0$ where $v_{g,x}$ represents the group velocity in the x direction.

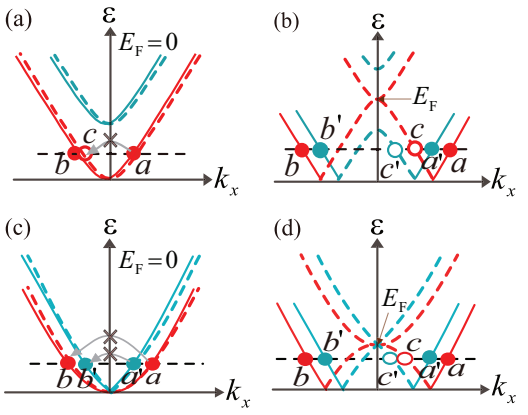

FIG. 4. (Color online) Excitation spectra at normal incidence, (a) and (b) for GML and (c) and (d) for GBL. (a) and (c) are plotted at $E_F = 0$, while (b) and (d) at $E_F \gg \Delta_0$. The solid and dashed lines indicate the subbands located, respectively, in valleys K and K′, and here electron excitations in K are coupled by the BdG equation to hole excitations in K′ (both valleys are needed because time-reversal symmetry is broken within one valley). The possible incident states ψ_a, $\psi_{a'}$ and the forbidden (×) reflected cases are denoted in panels (a) and (c). The incident state ψ_a, $\psi_{a'}$ and all of their possible reflected states are marked in panels (b) and (d).

After determining the subband indexes (μ,ν) for each incident and reflected state in N, the reflection process could be analyzed. Specifically at normal incidence, the dispersion at $E_F = 0$ is shown in Fig. 4(a). From Eq. (5), it is inferred that the specular Andreev reflection must be forbidden, because the reflected hole state ψ_c is orthogonal to the incident electron state ψ_a. Then on the equal-energy surface in Fig. 3(a), there is only one possible reflected state ψ_b that is nonorthogonal to ψ_a, and thus ψ_b is completely reflected. It is just the 2π-Berry phase of the spinor wave function that is responsible for this phenomenon. Another unusual point is that the reflected electron, at normal incidence, has the opposite spin with that of the incident electron, due to the spin helical structure of the equal-energy surface induced by RSOC. Such spin-flipped electron reflection does not occur at other graphene-based junctions previously studied [6,7,30–32], and can find its use in spintronic devices [33]. Figure 4(b) gives the dispersion at normal incidence under $E_F \gg \Delta_0$, where the electron reflection and Andreev retroreflection happen. Likewise, it can be verified that ψ_a ($\psi_{a'}$) is orthogonal to $\psi_{b'}$, $\psi_{c'}$ (ψ_b,ψ_c). The nonorthogonality of ψ_a and ψ_c suggests the existence of Andreev retroreflection. All these analyses from Figs. 4(a) and 4(b) reveal that an NS junction, based on GML with RSOC,

should display the same reflection phenomena with that based on GBL without RSOC [7], due to the 2π-Berry phase under $\lambda_R \neq 0$.

Graphene bilayer. By solving the BdG equation, the excitation spectrum ($\varepsilon_{\mu\nu} > 0$) of quasiparticles in region N read

$$\varepsilon_{\mu\nu} = \left| \frac{\hbar v_F k}{\gamma} \left(\sqrt{\lambda_R^2 + (\hbar v_F k)^2} - \nu \lambda_R \right) - \mu E_F \right|. \quad (17)$$

In comparison with Eq. (10), $\varepsilon_{\mu\nu} = |E_{\mu\nu}(k) - E_F|$. The Hamiltonian in S without RSOC simplifies to $\mathcal{H}_\xi(x > 0) = \mathcal{H}_\xi^0 - E_F'$. The excitation spectrum of the BdG quasiparticles can be given as $\varepsilon_{\mu\nu} = \sqrt{\Delta_0^2 + [E_F' + \mu(\hbar v_F k)^2/\gamma]^2}$. In both N and S, all the incident and interface-scattering states $(u,v)\exp(i\boldsymbol{k}\cdot r)$ in the Nambu space could be obtained by solving Eq. (15). Matching the wave functions at $x = 0$, all the reflection amplitudes can be calculated.

As described in GML, we will consider the Andreev reflections at an NS junction of GBL in the weakly doped regime I ($E_F < \Delta_0$) and strongly doped regime II ($E_F' \gg E_F \gg \Delta_0$). For the former, the specular Andreev reflection is present only when $\varepsilon > E_F$); for the latter, only Andreev retroreflection happens because $\varepsilon \ll E_F$. The Fermi energies E_F and E_F' in N and S could be tuned by doping [26]. Because a GBL with RSOC has no splitting of the four energy bands at point K or K′ [see Fig. 2(b)], two equal-energy incident states ψ_a, $\psi_{a'}$ always survive together, irrespective of which regime one operates. The equal-energy surfaces could also be described by Fig. 3(b), due to the identical spin helical structures of GML and GBL. The subband indices (μ,ν), however, change correspondingly: The incident states ψ_a, $\psi_{a'}$ lie in subbands $(+,+)$ and $(+,-)$, respectively; ψ_b and $\psi_{b'}$ describe the reflected electron states for ψ_a or $\psi_{a'}$; the reflected hole states ψ_c, $\psi_{c'}$ are contributed by subbands $(-,+)$ and $(-,-)$ [valence band in Fig. 2(b)] in regime I, whereas they are contributed by subbands $(+,+)$ and $(+,-)$ [conduction band in Fig. 2(b)] in regime II. Meanwhile, the incident and reflected particles should satisfy the momentum conservation in the y direction and have opposite directions of their group velocities in the x direction.

Particularly at normal incidence, we analyze the reflection process without calculation, after determining (μ,ν) for each incident and reflected state. The dispersion at $E_F = 0$ is displayed in Fig. 4(c). From Eq. (11), we find ψ_a ($\psi_{a'}$) is orthogonal to ψ_b ($\psi_{b'}$), due to the π-Berry phase at $\lambda_R \neq 0$. As a consequence, the corresponding electron reflections are suppressed, and the related specular Andreev reflections are enhanced. The other nonorthogonality of ψ_a and $\psi_{b'}$ ($\psi_{a'}$ and ψ_b) suggests the existence of scattering between two different subbands in addition to the specular Andreev reflection. It is inferred that the net signal of specular Andreev reflection at an NS junction based on GBL with RSOC is stronger than that in the case without RSOC, but it should be weaker than that happening at a GML NS junction [6] without scattering between different subbands. Figure 4(d) shows the dispersion under $E_F \gg \Delta_0$. In this situation, ψ_a ($\psi_{a'}$) is orthogonal to ψ_b, $\psi_{c'}$ ($\psi_{b'}$, ψ_c), and ψ_a ($\psi_{a'}$) is nonorthogonal to ψ_c ($\psi_{c'}$), and then the Andreev retroreflection is enhanced.

IV. SUBGAP DIFFERENTIAL CONDUCTANCE

As a result of spin splitting of energy bands induced by RSOC, we need to extend the Blonder-Tinkham-Klapwijk formalism [34] for a single-band incident state to the case of two incident states ψ_a, $\psi_{a'}$ in different subbands. The reflection amplitudes $(r_1,r_2,r_{A_1},r_{A_2})$, $(r_1',r_2',r_{A_1}',r_{A_2}')$ are, respectively, for the incident states ψ_a and $\psi_{a'}$, corresponding to their four shared reflected states ψ_b, $\psi_{b'}$, ψ_c, $\psi_{c'}$. The subgap ($eV < \Delta_0$) differential conductance is then written as

$$\frac{G}{G_0} = \frac{1}{\mathcal{N}_0} \int_0^{\pi/2} d\theta \cos\theta \big[\mathcal{N}_1 \big(1 - |r_1|^2 - P_{b'}|r_2|^2 + P_c |r_{A_1}|^2 + P_{c'}|r_{A_2}|^2\big) + \mathcal{N}_2 \big(1 - |r_1'|^2 - P_{b'}|r_2'|^2 + P_c |r_{A_1}'|^2 + P_{c'}|r_{A_2}'|^2\big)\big]. \quad (18)$$

The scaling coefficient $G_0 \equiv \partial I_0/\partial V = (2e^2/h)\mathcal{N}_0$ is the ballistic conductance of GML or GBL without RSOC, and the number of available channels $\mathcal{N}_0$ is determined by the bias eV and the dispersion. The channel numbers $\mathcal{N}_1$, $\mathcal{N}_2$ are for ψ_a, $\psi_{a'}$. The other coefficients take $P_{b'} = k_{b'}\cos\theta'/(k_a\cos\theta)$, $P_c = k_c\cos\theta_A/(k_a\cos\theta)$, $P_{c'} = k_{c'}\cos\theta_A'/(k_a\cos\theta)$, where (k_a,θ), $(k_{b'},\theta')$, (k_c,θ_A), $(k_{c'},\theta_A')$ are the wave-vector modulus and angles for the states ψ_a, $\psi_{b'}$, ψ_c, $\psi_{c'}$, determined by the conservation of energy and momentum at a given θ, as shown in Fig. 3 for GML.

Graphene monolayer. We now calculate the differential conductance at an NS junction based on a GML with width W using Eq. (18). According to the linear dispersion [6], it is obtained $\mathcal{N}_0 = (W/\pi)k = n_0(eV + E_F)$ with $n_0 = W/(\pi\hbar v_F)$. By taking $\mu = +(-)$, $\nu = +(-)$ in Eq. (16), $\mathcal{N}_{1(2)}$ is given as $\mathcal{N}_{1(2)} = n_0\sqrt{eV + E_F}\cdot\sqrt{eV + E_F + (-)\lambda_R}$. In regime I, ψ_a is the only incident state, and thus Eq. (18) reduces to $G/G_0 = (\mathcal{N}_1/\mathcal{N}_0)\int_0^{\pi/2} d\theta\cos\theta[1 - |r_1|^2 + P_1|r_{A_1}|^2]$, where the relation $|r_1|^2 + |r_{A_1}|^2 = 1$ holds. In regime II, because incident states ψ_a, $\psi_{a'}$ coexist and the scattering between different subbands exists, $\sum_{i=1}^2 |r_i|^2 + |r_{A_i}|^2 = 1$ and $\sum_{i=1}^2 |r_i'|^2 + |r_{A_i}'|^2 = 1$ hold, according to the particle conservation.

In Fig. 5(a), we plot the differential conductance against the bias voltage, at different Fermi energies $E_F/\Delta_0 = 0,0.5,50$, when the value of λ_R/Δ_0 is fixed at 20. For comparison, the differential conductance, at $\lambda_R = E_F/\Delta_0 = 0$ [6], is given here. As usual for an NS junction [35], the differential conductance always has a singularity at eV$= \Delta_0$. Comparing the results in the presence and absence of RSOC, at $E_F = 0$, it is found that the differential conductance is significantly lowered by the presence of RSOC, as expected, in contrast to the enhancement effect in magnetic graphene [12–15]. This is just the result of the topological change of the Berry phase, from π to 2π. Actually, this reversed Berry phase behavior results in a transition from constructive interference to destructive interference between the incident and specular Andreev reflection states. The curve for $E_F/\Delta_0 = 0.5$ can characterize the relation of conductance-bias voltage under $0 < E_F < \Delta_0$. The zero-bias conductance peak is contributed by the Andreev retroreflections, and the specular Andreev reflection dominates under eV $> 0.5\Delta_0$. At $E_F/\Delta_0 = 50$, the probabilities of the Andreev retroreflections, $|r_{A_1}|^2$ and $|r_{A_1}'|^2$, contribute most to the differential conductance. It is found

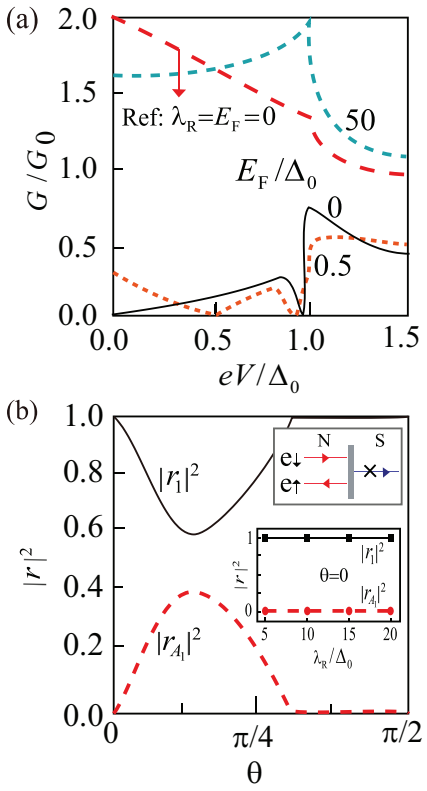

FIG. 5. (Color online) (a) Differential conductance vs bias voltage for GML. The curve at $\lambda_R = E_F/\Delta_0 = 0$ is for reference. The results, for $E_F/\Delta_0 = 0$, 0.5, 50, are plotted at $\lambda_R/\Delta_0 = 20$. (b) Reflection probabilities vs incident angle θ, at $\lambda_R/\Delta_0 = 20$, $E_F/\Delta_0 = 0.2$, $\varepsilon/\Delta_0 = 0.8$. The top right inset describes the allowed reflection and the forbidden transmission at $\theta = 0$, and the other inset gives the reflection probabilities vs λ_R at normal incidence.

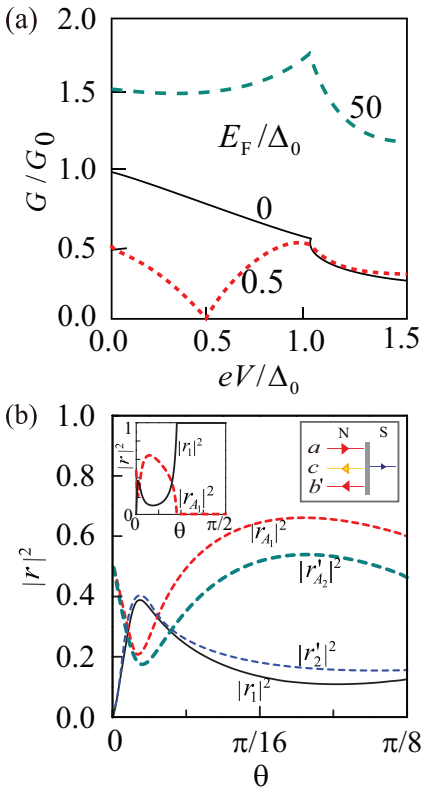

FIG. 6. (Color online) (a) Differential conductance vs bias voltage for GBL at $\lambda_R/\Delta_0 = 20$ and $E_F/\Delta_0 = 0$,0.5,50. (b) Reflection probabilities vs incident angle θ, at $\lambda_R/\Delta_0 = 20$, $E_F/\Delta_0 = 0.2$, $\varepsilon/\Delta_0 = 0.8$: $|r_1|^2$, $|r_{A_1}|^2$ are for the incident state ψ_a, and $|r'_2|^2$, $|r'_{A_2}|^2$ are for the incident state $\psi_{a'}$; $|r_1|^2$, $|r_{A_1}|^2$ vs the whole angle range $0 \leqslant \theta \leqslant \pi/2$ are given in the top left inset; the top right inset describes the interface scattering for the incident state ψ_a at $\theta = 0$.

that the differential conductance in Fig. 5(a) exhibits the same feature as displayed in the GBL-based NS junction without RSOC [7]. This demonstrates a topological equivalence, characterized by the same Berry phase 2π, between the GML with RSOC and the GBL without RSOC. In addition, a previous work [36] has proved that a strong topological correspondence exists between Andreev reflection and Klein tunneling in GML without RSOC. It can be inferred that the 2π-Berry phase here should be responsible for the origin of the results previously studied in integer quantum Hall effects [17] and Klein tunneling for GML with RSOC [37].

Considering that the differential conductance in Fig. 5(a) washes out those features upon angular integration in Eq. (18), it is necessary to display the reflection amplitudes against the incident angle θ. Figure 5(b) plots the probabilities $|r_1|^2$, $|r_{A_1}|^2$ vs the incident angle θ, for the intravalley electron reflection (solid line) and intervalley specular Andreev reflection (dashed line), at $E_F/\Delta_0 = 0.2$ and $\varepsilon/\Delta_0 = 0.8$. In line with the numerical result, the critical angle can be derived as $\theta_c = \arcsin\sqrt{\varepsilon_-(\varepsilon_- + \lambda_R)}/\sqrt{\varepsilon_+(\varepsilon_+ + \lambda_R)} \simeq 0.278\pi$ with $\varepsilon_\pm = \varepsilon \pm E_F$, beyond which the specular Andreev reflection is forbidden [7,32]. Note that the curve in Fig. 5(b) could show the main characteristics of reflections under $E_F \ll \Delta_0$. At $\theta = 0$, we also plot $|r_1|^2$, $|r_{A_1}|^2$ vs λ_R in the middle right inset of Fig. 5(b). It is shown that $|r_1|^2$ and $|r_{A_1}|^2$ are independent of λ_R because of the invariant 2π-Berry phase at any given nonzero λ_R here. Actually, the critical angle θ_c can be changed by different λ_R, and G/G_0 could change a little.

Graphene bilayer. We turn to calculate the differential conductance at an NS junction based on a GBL with width W using Eq. (18). At a given bias eV, parameters $\mathcal{N}_0$, $\mathcal{N}_1$, and $\mathcal{N}_2$ are solved as $\mathcal{N}_0 = n_0\sqrt{(\mathrm{eV} + E_F)\gamma}$ with $n_0 = W/(\pi\hbar v_F)$, and $\mathcal{N}_1 = (W/\pi)k_l$, $\mathcal{N}_2 = (W/\pi)k_m$. By taking $\mu = +(+)$, $\nu = +(-)$ in Eq. (17), the wave-vector modulus $k_{l(m)}$ could be solved by $(\mathrm{eV} + E_F)[\mathrm{eV} + E_F + (-)2\hbar v_F k_{l(m)}\lambda_R/\gamma] = [\hbar v_F k_{l(m)}]^4/\gamma^2$. The conductance G/G_0 vs the bias eV is plotted in Fig. 6(a), at $\lambda_R = 20\Delta_0$, when E_F in region N is fixed at 0 (solid line), 0.5 (short dashed line), 50 (long dashed line). As E_F/Δ_0 is tuned from 0 to 50, the dominant reflection varies from the specular Andreev reflection to the Andreev retroreflection. This result, like that occurring in GML without RSOC [6], originates from the π-Berry phase. Figure 6(b) further plots the reflection probability against the incident angle θ: The parameters are chosen at $E_F/\Delta_0 = 0.2$, $\varepsilon/\Delta_0 = 0.8$, the same as in Fig. 5(b), but the incident angle is limited to $\theta \leqslant \pi/8$ for showing precisely the main contribution to the conductance; in addition, for better comparison with Fig. 5(b), $|r_1|^2$ and $|r_{A_1}|^2$ vs the whole angle range $0 \leqslant \theta \leqslant \pi/2$ are given in the top left inset. It is shown that the probabilities

of electron reflections $|r_1|^2$, $|r_2'|^2$ are suppressed while the probabilities of the specular Andreev reflections $|r_{A_1}|^2$, $|r_{A_2}'|^2$ are enhanced. Moreover, just as in GML, one can prove that Andreev reflection has weak dependence on the value of nonzero λ_R.

In analogy with the GML without RSOC [6], the Rashba system of GBL exhibits the same phenomena of the specular Andreev reflection at an NS junction. This fact, in a certain sense, manifests the topological equivalence of these two systems. A notable difference is that multiband scattering processes exist in GBL with RSOC. The intravalley reflected electron, as indicated in the Rashba system of GML, can have flipped spin in comparison with that of the incident electron, due to the spin helical structures. Likewise, the Rashba system of GBL can be used in spintronic devices based on Andreev reflections [33].

Comparison between monolayer and bilayer. Comparing the results in Figs. 5 and 6, we can show that the presence of RSOC, in the weakly doped region N, leads to an anomalous result that the specular Andreev reflection is strongly suppressed for GML but observably enhanced for GBL. This reverse phenomenon originates from the topological reversal of the Berry phase, from π to 2π for GML and from 2π to π for GBL. Actually, the Berry phase here only describes a topology of electronic states at either K or K′ valley, but not the whole Brillouin zone. Because there exists no bulk band gap in the Rashba systems of GML and GBL, both the $\mathbb{Z}_2$ topological invariant [20,38] and the spin Chern number [39] are trivial. In this sense, the Berry phase here is a locally good topological invariant for these two Rashba systems. Additionally, if we consider a weak intrinsic spin-orbit coupling in GML and GBL with Rashba interaction [20,25,27], a bulk band gap may be opened, and the band topology could be very different due to the competition between Rashba and intrinsic spin-orbit couplings. The results discussed here might be affected, especially at very low energies.

Moreover, based on the fact that the Andreev reflection phenomena have been observed experimentally in graphene contacted by superconducting electrodes [8], there is the reason to believe that our predictions on the differential conductance can be verified. Besides, the previous measured 13-meV RSOC [18] is evaluated to be sufficient to validate our results, and the signal of differential conductance could be detected much easier in Rashba systems with a stronger RSOC up to 100 meV [40]. In turn, the experimental observations on differential conductance would provide an effective method to determine Berry phase. Further considering the availability of two-dimensional Rashba systems in designing topologically stable Majorana modes [41], there still needs to be more efforts to reach such a goal in graphene-based Rashba systems.

V. CONCLUSION

In summary, we have found both GML and GBL can exhibit nontrivial changes of their Berry phase, driven by RSOC, from π to 2π for GML but 2π to π for GBL. Such changes result in anomalous electron-hole conversions at NS junctions: The specular Andreev reflection is significantly reduced in GML, when region N is weakly doped, but obviously enhanced in GBL. Another unusual point caused by RSOC is that the spin-flipped electron reflection happens due to the special structures of spin helicities induced by RSOC. An electrically observable result is that the subgap differential conductance, driven by RSOC, exhibits a remarkable suppression in GML, but it displays an obvious enhancement in GBL. Our results provide new insight into the control of Andreev reflections and supercurrents in other kinds of superconducting heterojunctions by introducing RSOC.

ACKNOWLEDGMENTS

This work was supported by the State Key Program for Basic Research (Grant No. 2011CB922102), the Priority Academic Program Development of Jiangsu Higher Education Institutions (PAPD), and the National Natural Science Foundation of China (Grant No. 11074108).

[1] K. S. Novoselov, V. I. Fal'ko, L. Colombo, P. R. Gellert, M. G. Schwab, and K. Kim, Nature (London) **490**, 192 (2012).
[2] D. Pesin and A. H. MacDonald, Nat. Mater. **11**, 409 (2012).
[3] M. I. Katsnelson, K. S. Novoselov, and A. K. Geim, Nat. Phys. **2**, 620 (2006).
[4] K. S. Novoselov, E. McCann, S. V. Morozov, V. I. Fal'ko, M. I. Katsnelson, U. Zeitler, D. Jiang, F. Schedin, and A. K. Geim, Nat. Phys. **2**, 177 (2006).
[5] A. K. Geim and K. S. Novoselov, Nat. Mater. **6**, 183 (2007).
[6] C. W. J. Beenakker, Phys. Rev. Lett. **97**, 067007 (2006).
[7] T. Ludwig, Phys. Rev. B **75**, 195322 (2007).
[8] H. B. Heersche, P. Jarillo-Herrero, J. B. Oostinga, L. M. K. Vandersypen, and A. F. Morpurgo, Nature (London) **446**, 56 (2007).
[9] D. Rainis, F. Taddei, F. Dolcini, M. Polini, and R. Fazio, Phys. Rev. B **79**, 115131 (2009).
[10] Q.-F. Sun and X. C. Xie, J. Phys.: Condens. Matter **21**, 344204 (2009).
[11] W. J. Herrera, P. Burset, and A. L. Yeyati, J. Phys.: Condens. Matter **22**, 275304 (2010).
[12] M. Zareyan, H. Mohammadpour, and A. G. Moghaddam, Phys. Rev. B **78**, 193406 (2008).
[13] A. G. Moghaddam and M. Zareyan, Phys. Rev. B **78**, 115413 (2008).
[14] J. Linder, T. Yokoyama, D. Huertas-Hernando, and A. Sudbø, Phys. Rev. Lett. **100**, 187004 (2008).
[15] Q. Zhang, D. Fu, B. Wang, R. Zhang, and D. Y. Xing, Phys. Rev. Lett. **101**, 047005 (2008).
[16] B. Lv, C. Zhang, and Z. Ma, Phys. Rev. Lett. **108**, 077002 (2012).
[17] E. I. Rashba, Phys. Rev. B **79**, 161409(R) (2009).
[18] A. Varykhalov, J. Sánchez-Barriga, A. M. Shikin, C. Biswas, E. Vescovo, A. Rybkin, D. Marchenko, and O. Rader, Phys. Rev. Lett. **101**, 157601 (2008).
[19] Z. Qiao, W.-K. Tse, H. Jiang, Y. Yao, and Q. Niu, Phys. Rev. Lett. **107**, 256801 (2011).
[20] C. L. Kane and E. J. Mele, Phys. Rev. Lett. **95**, 146802 (2005).

[21] H. Suzuura and T. Ando, Phys. Rev. Lett. **89**, 266603 (2002).
[22] D. Xiao, M.-C. Chang, and Q. Niu, Rev. Mod. Phys. **82**, 1959 (2010).
[23] C.-H. Park and N. Marzari, Phys. Rev. B **84**, 205440 (2011).
[24] Y. Zhang, Y.-W. Tan, H. L. Stormer, and P. Kim, Nature (London) **438**, 201 (2005).
[25] X. Zhai and G. Jin, Spin **3**, 1330006 (2013).
[26] T. Ohta, A. Bostwick, T. Seyller, K. Horn, and E. Rotenberg, Science **313**, 951 (2006).
[27] G. P. Miktik and Yu. V. Sharlai, Low Temp. Phys. **34**, 794 (2008).
[28] F. Mireles and J. Schliemann, New J. Phys. **14**, 093026 (2012).
[29] M. Koshino and E. McCann, Phys. Rev. B **80**, 165409 (2009).
[30] Y. Asano, T. Yoshida, Y. Tanaka, and A. A. Golubov, Phys. Rev. B **78**, 014514 (2008).
[31] M. J. M. de Jong and C. W. J. Beenakker, Phys. Rev. Lett. **74**, 1657 (1995).
[32] J. Linder and A. Sudbø, Phys. Rev. B **77**, 064507 (2008).
[33] I. Žutić, J. Fabian, and S. Das Sarma, Rev. Mod. Phys. **76**, 323 (2004).
[34] G. E. Blonder, M. Tinkham, and T. M. Klapwijk, Phys. Rev. B **25**, 4515 (1982).
[35] M. Tinkham, *Introduction to Superconductivity* (Dover, New York, 2004).
[36] C. W. J. Beenakker, A. R. Akhmerov, P. Recher, and J. Tworzydło, Phys. Rev. B **77**, 075409 (2008).
[37] M.-H. Liu, J. Bundesmann, and K. Richter, Phys. Rev. B **85**, 085406 (2012).
[38] X. Zhai and G. Jin, Appl. Phys. Lett. **102**, 023104 (2013).
[39] E. Prodan, Phys. Rev. B **80**, 125327 (2009).
[40] D. Marchenko, A. Varykhalov, M. R. Scholz, G. Bihlmayer, E. I. Rashba, A. Rybkin, A. M. Shikin, and O. Rader, Nat. Commun. **3**, 1232 (2012).
[41] S. Nakosai, Y. Tanaka, and N. Nagaosa, Phys. Rev. Lett. **108**, 147003 (2012).